Thermal-Comfort Design of Personalized Casts

Xiaoting Zhang[1]   Guoxin Fang[2]   Chengkai Dai[2]   Jouke Verlinden[2]
Jun Wu[2]   Emily Whiting[1]   Charlie C.L. Wang[2]

[1]Boston University   [2]TU Delft

ABSTRACT

This paper introduces a novel method for designing personalized orthopedic casts which are aware of thermal-comfort while satisfying mechanical requirements. Our pipeline starts from thermal images taken by an infrared camera, by which the distribution of thermal-comfort sensitivity is generated on the surface of a 3D scanned model. We formulate a hollowed Voronoi tessellation pattern to represent the covered region for a web-like cast design. The pattern is further optimized according to the thermal-comfort sensitivity calculated from thermal images. Working together with a thickness variation method, we generate a solid model for a personalized cast maximizing both thermal comfort and mechanical stiffness. To demonstrate the effectiveness of our approach, 3D printed models of personalized casts are tested on body parts of different individuals.

ACM Classification Keywords

D.2.2 Software Engineering: Design Tools and Techniques—Object-oriented Design Methods; J.6 Computer Applications: Computer-Aided Engineering—Computer-Aided Manufacturing (CAM)

Author Keywords

personalized cast; thermal-comfort; 3D printing; pattern optimization; structural analysis

INTRODUCTION

An orthopedic cast is a shell encasing portions of the human body to stabilize and immobilize broken or dislocated bones for rehabilitation. Traditional casts are made from plaster or fiberglass together with a soft inner cotton layer. These materials have poor breathability and are not water resistant. As a result, skin can become irritated and in some scenarios, cutaneous complications can occur. With the advent of the digital manufacturing era, state-of-the-art technologies in 3D scanning and 3D printing have been applied in surgical practices and orthopedic treatment [33]. A digital 3D human body model reconstructed by 3D scanning can be printed for a variety of innovative uses such as preoperative planning [18], customized implant fabrication [11] and patient specific instruments [50].

Figure 1. We propose a new method for thermal-comfort design of personalized casts. (Left) Physical-data acquisition by a 3D scanner and a thermal camera. (Right) Comparison of skin temperature on uniform skin exposure (left) vs. our optimized cast (right). Two casts have the same area of skin exposure.

While the advantages of 3D printed casts with customized shapes and ensured mechanical stiffness have been well recognized in biomedical applications (e.g., [21, 27]), research also shows that thermal sensitivity varies at different regions of a human body [54]. Moreover, it is found that the distribution of thermal sensitivity also changes from person to person [24], e.g., one individual could be very sensitive to heat at the forearm while another could be more sensitive at the wrist. The same observation is found in our experimental tests – the same region of skin on different individuals can have different temperature variations (see Fig. 3). *Thermal-comfort*, as a sensation describing how people feel about the thermal state of the body, can be improved by customizing the air-exposure of skin in regions with high thermal sensitivity. As a result, skin irritation and infection are less likely to occur [27]. In summary, the design of a cast should be customized in terms of shape, mechanical stiffness and also thermal-comfort. Prior work mainly addresses this multi-physics based design problem empirically. In contrast, we propose a new computational approach to tackle this design challenge of personalized products (see Fig.1).

Our pipeline is illustrated in Fig. 2. The input of the system is a scanned 3D model and the thermal images taken by an infrared camera. We first generate the temperature distribution by mapping the thermal images onto the 3D model. Then, thermal-comfort sensitivity is computed to govern the pattern generation, where human thermal-comfort is maximized. Considering factors of aesthetics and structural strength, a *Hollowed Voronoi Tessellation* (HVT) pattern is employed for designing a web-like pattern. After optimizing the pattern for air-exposure, a structural enhancement scheme is performed

to convert the HVT surface into a solid model that ensures mechanical stiffness on the cast with thicker shells being used at structurally weaker regions.

We validate our method by comparing thermal images of individuals after wearing an optimized cast and a uniform cast. As shown in Fig.1, the optimized cast achieves a lower temperature distribution than the uniform cast. Physical tests are performed on different body parts of four participants. Two experimental environments with different temperatures (i.e., an office room and a sauna room) are set to demonstrate the consistency of our method. Positive feedback from these participants confirms a better user experience, compared with wearing non-optimized casts.

We make three main contributions in this work:

- We present a workflow for customized cast fabrication wherein casts are made based on personal heat distribution.

- We introduce an optimization algorithm for cast design to maximize thermal-comfort of the user while ensuring mechanical stiffness of the cast.

- We implement a cast design system and demonstrate the effectiveness on example applications.

To the best of our knowledge, no prior method exists addressing the thermal-comfort problem on a wearable instrument. Our work currently focuses on designing web-like casts, which can be extended to thermal-comfort aware design of other personalized wearable instruments (such as braces, helmets, etc.).

RELATED WORK

Personal Fabrication Personal fabrication is an emerging research topic in computer human interaction and related disciplines [6]. Laput et al. [23] exploited the stringing phenomena in 3D FDM printers to fabricate hair, fibers and gristles. Recently, a 3D scanning and printing system was developed to enable product design using physical annotations [40]. Mueller et al. [36] combine LEGO blocks and 3D printing to fabricate models in reduced times. WirePrint [35] fabricates the edges of a triangular mesh model by 3D printing for the purpose of preview. To reduce the consumption of materials, a fabrication system [45] was developed to use parts of existing models by integrating 3D scanning, milling and printing. In particular, there has been a recent focus on fabricating artifacts around a human body. Tactum [16] uses skin as the input surface and captures users' gestures for 3D digital modeling and fabrication. ExoSkin [17] prints 3D models on the human body by a hand-held extruder. Torres et al. [46] enabled physical haptic design in 3D printing to change the feel, usability and interactivity of objects. Our research enriches the area of personal fabrication by considering thermal-comfort of 3D printed wearable instruments.

3D Printed Casts Recently, 3D printed orthopedic casts as customized rehabilitation tools have been developed in the design community to address limitations of traditional casts. A 3D printed plastic cast is waterproof, and porous structures can be designed to make it ventilated, lightweight and hygienic [27]. Evill [14] designed a web-like cast named *Cortex* with

denser mesh at the region of bone fracture to provide support. Karasahin [20] created a similar cast named *Osteoid* equipped with a low intensity pulsed ultrasound bone simulator system. Efforts were also made in [21, 27] to predict the mechanical performance of a 3D printed cast by using *Finite Element Analysis* (FEA). However, existing approaches involve heavy manual editing of 3D models – which is time-consuming and requires experienced CAD engineers. Furthermore, thermal-comfort is not considered. To address these problems, we propose a computational solution to automate the design of thermal-comfort and structurally-sound casts.

Designing Structural Patterns Several design tools have been proposed to design structural patterns on shells, mainly motivated by decorative purposes. Dumas et al. [13] proposed a structural synthesis method to generate a large surface pattern from a user-specified pattern example. Martínez et al. [32] integrated structural synthesis with topology optimization to optimize shapes regarding both their structural properties and their appearance. Chen et al. [10] proposed a filigree synthesis method, equipped with a stochastic optimization strategy, to automate the design of visually appealing and fully connected filigrees. Schumacher et al. [42] proposed a method to design shells with artistic cutouts. The distribution and scaling of these stencils are optimized for aesthetics, stability, and material efficiency. Zehnder et al. [53] proposed a computational tool for designing curve networks on surfaces, taking user-defined spline curves as central design primitives. Volumetric patterns such as skin-frame structures [48], honeycomb structures [30] and self-supporting rhombic structures [52] have been proposed for designing lightweight infill in 3D printed models. Our work is related in the sense that we generate a sparse geometric pattern on the shell. However, besides expressiveness of the generated patterns, the design of personalized casts additionally requires considering thermal-comfort of the pattern, necessitating accurate modelling of thermal and structural properties.

Structural Strength Analysis Stress analysis is an integral part in design and optimization of structures. FEA has been employed broadly in design tools. FEA is computation intensive, especially as fine geometric details from structural synthesis necessitate a high-resolution geometric discretization, leading to millions of finite elements. To provide interactive design, a number of techniques have been employed, including numerical homogenization [38, 41, 31], geometric multi-grid solvers on the GPU [51], worst-case structural analysis [56], data-driven finite elements [9], local subspace projection [37], and stochastic structural analysis [22]. The multi-grid FEA solver [51] is employed in our optimization routine to efficiently evaluate the mechanical properties of the cast model.

HUMAN THERMAL SENSATION AND COMFORT

Thermal-comfort, as a sensation, describes how people feel about the thermal state of the body. ASHRAE [3] defines it as the satisfactory condition of mind expressed with the thermal environment, which is usually evaluated in a perceptual manner. Prior studies show that sensation and comfort are strongly correlated in *uniform* environments (i.e., with no
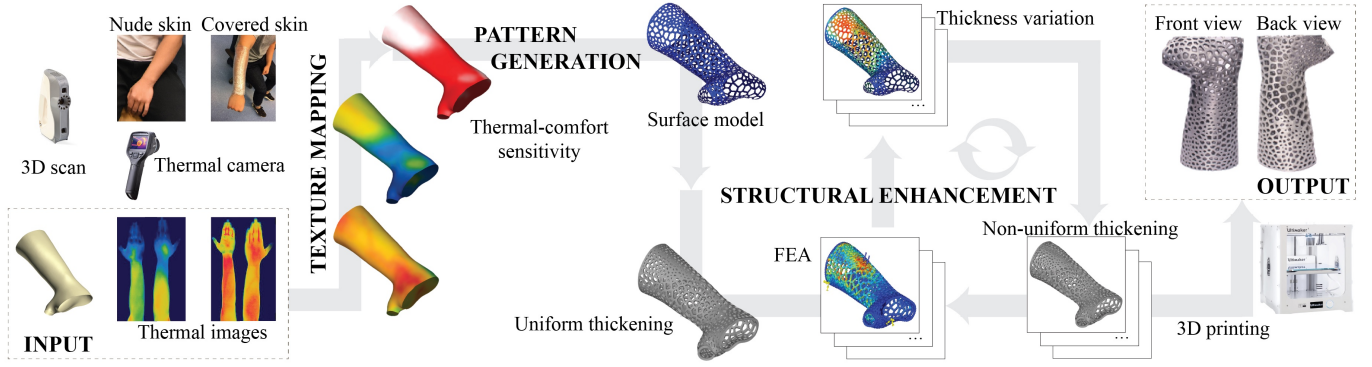
Figure 2. Pipeline for thermal-comfort design of personalized casts.

Table 1. Scales for Thermal Sensation and Comfort [55]

Index	Thermal Sensation	Index	Thermal Comfort
4	very hot	4	very comfortable
3	hot	2	comfortable
2	warm	+0	just comfortable
1	slightly warm	-0	just uncomfortable
0	neutral	-2	uncomfortable
-1	slightly cool	-4	very uncomfortable
-2	cool		
-3	cold		
-4	very cold		

change in environmental temperature). Specifically, a neutral sensation corresponds to the best comfort and warmer (or cooler) sensations lead to less comfort [15].

To evaluate thermal sensation and comfort, a widely used method is to collect ratings from subjects about their satisfaction – e.g., in [2], a 9-point scale is used for thermal sensation and a 6-point scale is employed for thermal comfort (as shown in Table 1). Note that 'very comfortable' is more prone to be perceived when a thermal stimulus applied to a local body part serves to reduce whole-body thermal stress, which is more likely to happen under asymmetrical and transient environments [34, 4]. It is also observed that thermal-comfort is a piecewise linear function of thermal sensation under uniform environments. Furthermore, according to experiments, local sensation is not only influenced by local skin temperature but also by overall temperature of the body. A mathematical function has been proposed in [54] to describe the relationship between local body sensation $S(\mathbf{x})$ and skin temperature $T(\mathbf{x})$ at a point $\mathbf{x}$ on the body in a uniform environment as

$$S(\mathbf{x}) = \frac{8}{1 + e^{-\alpha(T(\mathbf{x})-\tau(\mathbf{x}))-\beta[(T(\mathbf{x})-\tau(\mathbf{x}))-(\bar{T}-\bar{\tau})]}} - 4 \quad (1)$$
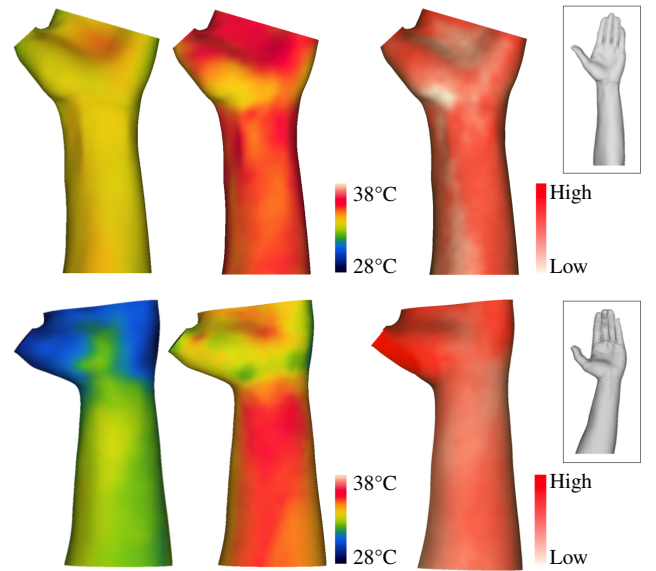

Figure 3. Our personalized cast design accounts for variations among individuals in both 3D shape and thermal-comfort sensitivity. Top and bottom rows are thermal data measured on different individuals. (Left, Middle) Temperature distributions under different conditions: neutral nude $\tau(\mathbf{x})$ (left) and completely covered $T(\mathbf{x})$ (middle). Temperatures are measured immediately after uncovering. (Right) Different distributions of thermal-comfort sensitivity $C(\mathbf{x})$ can be observed.

where the local sensation $S(\mathbf{x})$ ranges from very cold (-4) to very hot (4). $\tau(\mathbf{x})$ is the local skin temperature when the sensation of the local body part feels neutral, $\bar{T}$ is the average skin temperature over the whole body, and $\bar{\tau}$ gives the average skin temperature when the whole body feels neutral. α and β are specific regression coefficients for different body parts. Motivated by Zhang et al. [54], we propose a set of physical-data acquisition steps to generate a distribution of thermal-comfort sensitivity on the human body, which will be used to compute a 'good' pattern for the cast design.

Thermal-Comfort Sensitivity Here we focus on the distribution of thermal-comfort sensitivity. Two temperature distributions will be measured on a human body in a uniform environment: i) $\tau(\mathbf{x})$ on nude skin when the human body
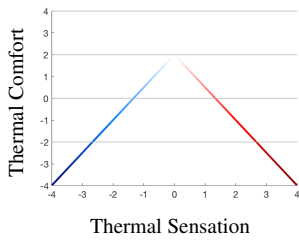
feels neutral, and ii) $T(\mathbf{x})$ on fully covered skin[1]. The following assumptions are made to simplify the complex thermo-physiological prediction.

- *Assumption I:* Considering only a relatively small region is covered by the cast, it is assumed that the change of the whole body temperature by wearing a cast is negligible (i.e., $\bar{T} = \bar{\tau}$ in Eq.(1)).

- *Assumption II:* Skin temperature of the covered parts is only affected by convective heat transfer with the surrounding space, but not the physical interactions (e.g. basal blood circulation) with the human body (ref. [1]).

Based upon these assumptions, the comfort sensitivity C of the human body is a piecewise linear function of thermal sensation – the bigger the temperature variation the more sensitive. Incorporating the condition that $T(\mathbf{x}) \geq \tau(\mathbf{x})$ in our application, the distribution of thermal-comfort sensitivity can be formulated as

$$C(\mathbf{x}) = \frac{12}{1 + e^{-\alpha(T(\mathbf{x}) - \tau(\mathbf{x}))}} - 8 \tag{2}$$

with $\alpha = 0.7$ for the forearm, $\alpha = 1.25$ for the neck and $\alpha = 0.4$ for the lower leg following the thermal sensation models introduced in [54], where 19 coefficients are given in different regions of a human body according to the regression computed from 22 specimens. A thermal energy term will be derived from this thermal-comfort sensitivity to govern the pattern optimization.

Physical-Data Acquisition Two distributions of temperature on the skin of a human body, $T(\mathbf{x})$ and $\tau(\mathbf{x})$, need to be obtained together with its 3D shape H as the input to our framework. We use a structured-light 3D scanner to obtain the geometry of H. The thermal images captured by an infrared camera are converted into a 2D temperature distribution, which are mapped onto the 3D model to generate the temperature distributions. In the first step of data acquisition, the thermal images of $T(\mathbf{x})$ are captured on nude skin. We then wrap plastic film around the local body part for 30 minutes. Under the same environmental temperature the images of $\tau(\mathbf{x})$ are captured immediately after uncovering the plastic film. Through these steps, we are able to obtain $T(\mathbf{x})$ and $\tau(\mathbf{x})$ and generate a distribution of thermal-comfort sensitivity by Eq.(2). An example can be found in Fig.3. Given $C(\mathbf{x})$, we then generate the thermal-comfort cast pattern, detailed in the following section.

PATTERN OPTIMIZATION

In order to maximize thermal-comfort, our system generates patterns with more air exposure at thermally sensitive regions. This can be achieved by generating a mesh with an adaptive cell distribution. We formulate the problem as an optimization. Given a surface of a scanned 3D body, we propose a new *Hollowed Voronoi Tessellation* (HVT) pattern for web-like casts. Each Voronoi cell is hollowed by removing the cell's center. Our pattern optimization changes the distribution and size of Voronoi cells by shifting the centers of cells so

[1]Note that the image of $T(\mathbf{x})$ can be measured by an infrared camera immediately after uncovering.
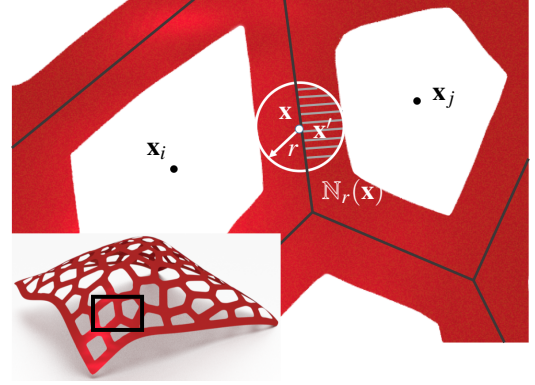

Figure 4. The hollowed Voronoi tessellation on a surface patch – shaded area is a region around the edges of the Voronoi tessellation that gives a nonzero value for the characteristic function (as defined in Eq. (3)).

that skin regions more sensitive to thermal comfort are more exposed. We define two energy terms – the thermal-energy term increases air exposure to thermally sensitive skin regions and the pattern-control term results in structures similar to honeycombs. The optimized distribution and sizes of holes are obtained based on Lloyd's method [28] by iteratively moving the centers of Voronoi cells to minimize the energy function.

Hollowed Voronoi Tessellation

We introduce a Hollowed Voronoi Tessellation to generate cast patterns. A local characteristic function is defined on the Voronoi cells that indicates the hollowed region. Given a set of generators (or seeds) $\{\mathbf{x}_i\}_{i=1}^{n}$, traditional Voronoi tessellation indicates that the Voronoi cell ψ_i on the surface M corresponding to the generator $\mathbf{x}_i$ is defined as the set of every point $\mathbf{x}$ on the surface whose distance to $\mathbf{x}_i$ is not greater than the distance to any other seeds $\mathbf{x}_j$. With the Voronoi tessellation $\Psi = \{\psi_i\}_{i=1}^{n}$, we define a local neighborhood $\mathbb{N}_r(\mathbf{x})$ with radius r, where any point $\mathbf{x}' \in \mathbb{N}_r(\mathbf{x})$ is a neighbor of $\mathbf{x}$. HVT can then be defined with the help of a local characteristic function $L_\Psi(\mathbf{x})$. The function returns a value to indicate whether a point's distance to the boundary of a voronoi cell is less than r – one for true and zero for false.

$$L_\Psi(\mathbf{x}) = \begin{cases} 1, & \text{if } \mathbf{x} \in \psi_i, \text{ and } \exists\, \mathbf{x}' \in \psi_{j\,(j \neq i)} \text{ where } \mathbf{x}' \in \mathbb{N}_r(\mathbf{x}) \\ 0, & \text{otherwise} \end{cases}, \tag{3}$$

The surface of a HVT is then defined as $P_\Psi = \{\mathbf{x} \in M \mid L_\Psi(\mathbf{x}) = 1\}$. An illustration for HVT can be found in Fig. 4.

Thermal Energy In the modeling pipeline of our approach, the porous HVT surface P_Ψ will be extruded along the surface normal direction to become a solid Q_Ψ. Skin of a user wearing the cast is only covered in the region of P_Ψ, while the other regions $M \setminus P_\Psi$ of the skin are exposed to air and have good ventilation, i.e., will not generate discomfort. The level of thermal-comfort according to a HVT can then be evaluated by

a thermal energy as

$$E_T(\Psi) = \int_{P_\Psi} C(\mathbf{x})d\mathbf{x} = \int_M C(\mathbf{x})L_\Psi(\mathbf{x})d\mathbf{x}, \qquad (4)$$

which is an integral of thermal-comfort sensitivity in those covered regions. With a fixed width r, different distributions of generators in Voronoi tessellations result in different values of $E_T(\Psi)$. For those with sparse generators at regions with high thermal-comfort sensitivity, bigger holes will be generated on the solid cast – therefore more skin-air ventilation will occur. As a result, users feel more comfortable.

Minimizing the thermal energy defined above will lead to a distribution of generators, $\{\mathbf{x}_i\}$, maximizing the thermal-comfort. However, a straightforward formulation of $\{\mathbf{x}_i\} = \arg\min E_T(\Psi)$ will lead to a trivial solution – locating all generators at a region with minimal $C(\mathbf{x})$. To solve this problem, we add a pattern control term in our framework.

Pattern Control   For our application of personalized casts, a mechanically stable structure needs to be used in the design. *Centroidal Voronoi tessellation* (CVT) with L^2-norm distance metric is chosen here because it can result in structures similar to honeycombs, which shares the target mechanical properties in lightweight and specific strength [7]. CVT is a special kind of Voronoi tessellation that the generator $\mathbf{x}_i$ of each cell ψ_i is also its center of mass. That is

$$\mathbf{x}_i = \mathbf{c}_i = \int_{\psi_i} \rho(\mathbf{x})\mathbf{x}d\mathbf{x} \Big/ \int_{\psi_i} \rho(\mathbf{x})d\mathbf{x} \qquad (5)$$

where $\rho(\mathbf{x})$ is a density function that can differ for different applications. The construction of CVT can also be considered as an energy minimization process [12]

$$E_P(\Psi) = \sum_{i=1}^{n} \int_{\psi_i} \rho(\mathbf{x})d(\mathbf{x}, \mathbf{x}_i)d\mathbf{x} \qquad (6)$$

$E_P(\Psi)$ is minimized only if $\{\mathbf{x}_i\}$ forms a CVT. Especially, when a constant $\rho(\mathbf{x})$ is used, a uniform CVT will be constructed for Ψ. When different distance metrics are used for $d(\cdot,\cdot)$, different patterns of CVT can be formed [25]. To obtain the nice properties of honeycomb structures, the geodesic distance is used for $d(\cdot,\cdot)$ in our approach.

Framework of Computation   Thermal-comfort aware pattern optimization is formulated as minimizing a total energy that is composed of a thermal term and a pattern control term

$$\hat{E}(\Psi) = E_P(\Psi) + \lambda E_T(\Psi), \qquad (7)$$

where a contrast coefficient λ is used to control the relative density of Voronoi cells in different regions (e.g., $\lambda = 75$ is used in most of the examples in this paper). Given a surface M, without loss of generality, we assume M is represented as a two-manifold triangular mesh with very small and dense facets. A Voronoi tessellation can be computed on the surface by using triangles as the elementary primitives – with a given set of generators $X = \{\mathbf{x}_i\}_{i=1}^n$, each triangle f is assigned to a Voronoi cell ψ_i when the distance from $\mathbf{x}_i$ to the center of f is not larger than any other generators.

Lloyd's method [28] is the most popular numerical implementation of the classic CVT problem. In our application,
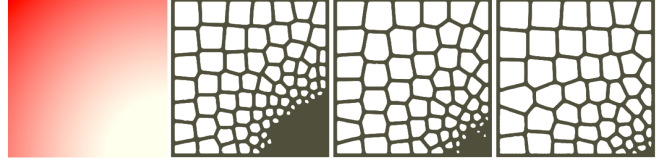

Figure 5. Progressive results of HVT variation during the computation. From left to right, a given thermal-comfort sensitivity, the initial HVT with 200 generators ($A(P_\Psi) = 0.4145A(M)$), a temporary result with the number of generators reduced to 100 ($A(P_\Psi) = 0.3445A(M)$), and the final converged result with 54 cells ($A(P_\Psi) = 0.3076A(M)$).
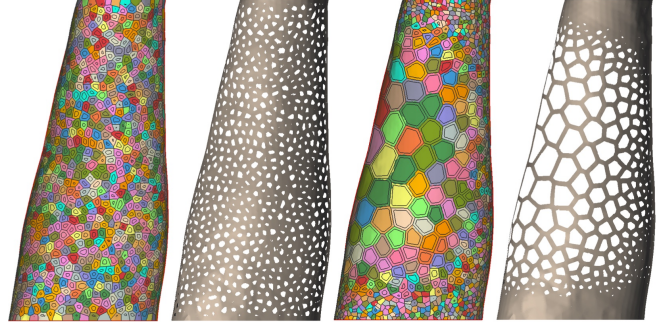

Figure 6. Some regions will be completely covered if the cell-removal mechanism is not included in our algorithm. (Left) a cast with uniform distribution of 500 cells, and (right) a cast with the same number of cells but having adaptive distribution. As a result, discomfort at fully covered regions (although having low thermal-comfort sensitivity) will dominate the overall perception of comfort.

we propose a variation of Lloyd's method that uses the total energy in Eq.(7) to guide the tessellation. Our algorithm adaptively changes the number of seeds to avoid non-hollowable cells during the iteration. Starting from n generators randomly selected on the surface, our algorithm repeatedly executes the following steps

1. Compute a CVT by the generators – determine the membership for all triangles on the surface;

2. Each triangle is reassigned to the Voronoi cell ψ_i reducing the total energy $\hat{E}(\Psi)$ in Eq.(7);

3. Compute the new positions of all generators $\{\mathbf{x}_i\}_{i=1}^n$ by Eq.(5);

4. Remove the small cells which are not able to be hollowed by eliminating their generators.

5. Terminate if no generator has a new position in this iteration; otherwise, go back to step 2.

Our algorithm can effectively optimize the distribution of HVT for thermal-comfort (see Fig. 5 for an example in 2D). The small cell removal steps are very important to keep a good skin-air ventilation condition at all regions. Without the step of small cell removal, some regions of skin will be completely covered, which results in discomfort even at in places with low thermal-comfort sensitivity (see Fig. 6).
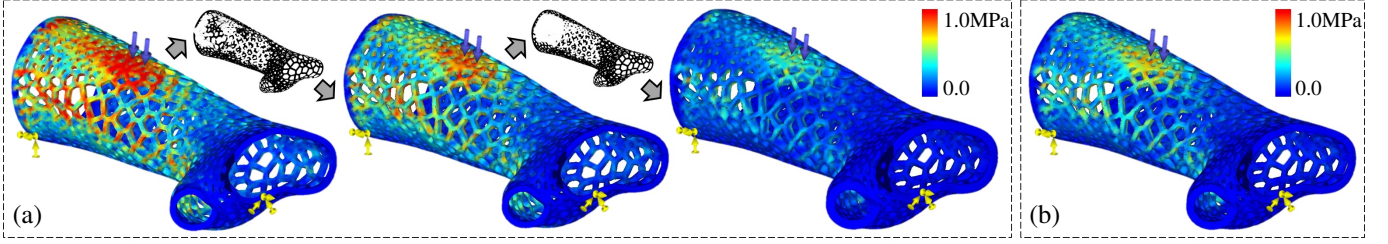
Figure 7. **Structural enhancement.** (a) Starting from $t_{\min} = 4\text{mm}$ (left), the distribution of non-uniform thickness is iteratively updated until the maximal stress on the cast is less than $\bar{\sigma}$ (right), where $t_{\max} = \max(t(\mathbf{x})) = 6mm$. (b) Cast with uniform thickness of $5.6mm$ having the same total weight as the optimized cast in (a). In comparison, the optimized cast has smaller maximal stress.

STRUCTURAL ENHANCEMENT

Casts require a certain stiffness to support the fractured bones. To enhance stiffness while preserving material, we propose a variable thickness.

The solid model of a cast, Q_Ψ, for an optimized HVT pattern Ψ can be extruded from its corresponding surface patch P_Ψ with a given thickness t_c. However, an intuitively chosen value for thickness can result in a solid either too heavy or too weak. By including *Finite Element Analysis* (FEA) in the loop of computation, we develop a method to iteratively determine a non-uniform distribution of $t(\mathbf{x})$ ($\forall \mathbf{x} \in P_\Psi$) using 3-point bending test, which is a standard method to study the strength of a cast [43]. Our structure enhancement ensures the maximal stress in the solid model is less than a critical threshold to prevent possible mobilization or even fracture. Note that, the extrusion for converting P_Ψ into a solid Q_Ψ along the surface normals on M can keep the dimension of holes on P_Ψ. Therefore, the thermal-comfort of a cast will not be affected by the variation in thickness unless an extreme extrusion length is applied. We control the variation of thickness as $t(\mathbf{x}) \in [t_{\min}, t_{\max}]$.

Non-uniform Thickness for Structural Enhancement The distribution of non-uniform thickness is computed according to the structural analysis. First of all, a uniform thickness is applied to generate Q_Ψ by letting $t(\mathbf{x}) = t_{\min}$ ($\forall \mathbf{x} \in P_\Psi$). FEA is then conducted on the solid model with the boundary condition of 3-point bending (see Fig.7). The stresses on Q_Ψ are then studied. For any place $\mathbf{q} \in Q_\Psi$ with its stress $\sigma_\mathbf{q}$ larger than the criterion $\bar{\sigma}$, the closest point of $\mathbf{q}$ on the patch P_Ψ is added into a set of risky points, R. Then, an updated field of thickness $t(\mathbf{x})$ is computed as a Harmonic field [5] with constraints on the boundary points and the risky points as

$$\nabla^2 t(\mathbf{x}) = 0$$
$$s.t. \quad t(\mathbf{x}) = t^{prev}(\mathbf{x}) + \delta t \quad (\forall \mathbf{x} \in R), \quad (8)$$
$$t(\mathbf{x}) = t_{\min} \quad (\forall \mathbf{x} \in (\partial M \setminus R))$$

where $t^{prev}(\cdot)$ gives the thickness at a point in the previous iteration. After obtaining a new $t(\mathbf{x})$, the new solid can be generated to perform FEA again. The field of thickness is incrementally updated in this way until $R = \emptyset$ – see Fig.7 for progressive results on an example.

As the solid extruded from a patch of HVT pattern has many small features, perfect volumetric meshes required by conven-

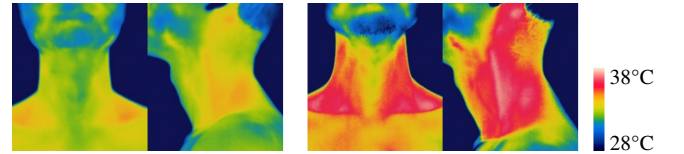**Figure 8. Two experimental environments. (Left)** an office, and **(right)** a sauna room.

Figure 9. Two sets of photos taken as input for thermal-comfort design. (Left) neutral nude skin, and **(right)** skin after being locally wrapped with plastic film for 30 minutes. Both are measured under the same office temperature at 23°C.

tional FEA packages can hardly be generated. A voxel-based FEA package [51] is employed in our paradigm to conduct the structural analysis – the resolution of voxels is set as 256^3 with each voxel's width as 1mm. All examples in this paper start from the thickness $t_{\min} = 4\text{mm}$. When incrementally changing the field of thickness, $\delta t = 0.5\text{mm}$ is used.

Solids with Variational Thickness The solid Q_Ψ with non-uniform thickness $t(\mathbf{x})$ is computed from P_Ψ with the help of a scaled signed distance field. Following the definition given in [47], an implicit representation of the solid is defined on a regular grid in 3D space, where each node of the grid stores a binary value to indicate whether the node is inside the solid. The non-uniform thickness distribution is defined by a nonlinear scaling approximation—in our implementation, a cubic Bernstein function is used. The mesh surface of a resulting solid can be obtained by a polygonization method (e.g., Marching Cubes [29] or Dual Contouring [19] algorithms).
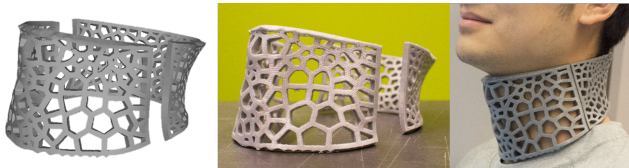
Figure 10. Optimized neck cast in two pieces. (Left) Digital model, and (right) 3D printed neck cast worn by the user.

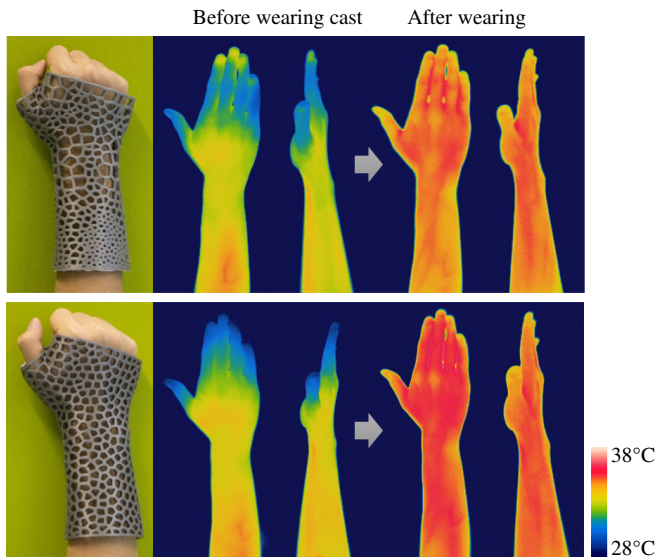Before wearing cast   After wearing

38°C
28°C

Figure 11. Physical experiments of the participant A. Wearing an optimized cast (top) and a uniformly-sparse cast (bottom) in an office room for 30 minutes. Skin temperature is lower for the optimized cast.

RESULTS

We now describe the experimental validation and analysis of our approach. Experimental tests are performed on four participants with different body parts and body shapes. 3D geometric models of their bodies are scanned by an Artec Eva 3D scanner, and a FLIR E60 infrared camera is used to generate the thermal images. Computations are performed on a MacBook with 2.8 GHz Intel Core i7 and 16 GB RAM. For physical verification, the solid models of casts are fabricated on an Ultimaker 3D printer using *polylactide* (PLA) material.

Environmental Setting   Two experimental environments are employed (see Fig. 8). One is an office room with air conditioning where the temperature is adjusted to 23°C. To examine thermal-comfort in extreme conditions, the second test environment is a sauna room with the temperature set to 40°C. The input thermal-images are captured as described in the Physical-Data Acquisition section. The resultant thermal-images are taken immediately after removing the casts (see Fig. 9 for example input for the neck cast design).

Fabrication   The solid models generated by our approach were directly sent to a 3D printer for fabrication. For a cast model with a dimension of $82 \times 102 \times 179$ mm^3, the printing time could be up to 22 hours. To make the cast wearable, we divided the cast model into two interlocking halves using smart 'invisible' interlocks introduced by Evill [14]. We first subdivide the surface model of the human body into two pieces
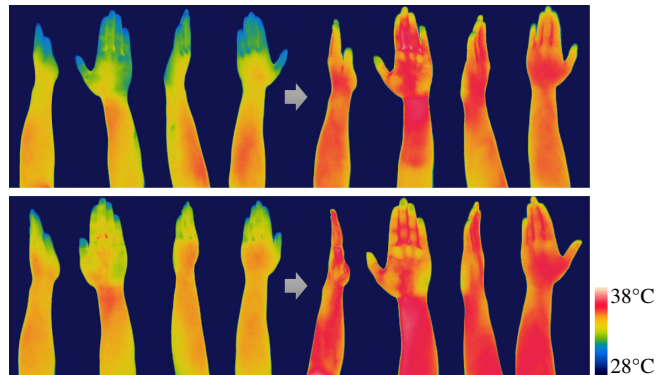

38°C
28°C

Figure 12. Comparison of temperature distribution after participant B wears an optimized cast (top) vs. a uniformly-sparse cast (bottom) in a sauna room for 30 minutes.

that can be disassembled, and then compute the optimized HVT and thereafter the resultant solid on each of these pieces (see Fig.10 for an illustration). The dimensions and weights of optimized casts are listed below.

Cast	Figure	Dimensions (mm^3)	Weight (g)
Right Arm	11	$82 \times 102 \times 179$	117
Left Arm	12	$77 \times 89 \times 183$	123
Neck	13	$147 \times 133 \times 92$	96
Right Leg	14	$164 \times 234 \times 189$	154

Thermal Verification   Physical tests were performed on different body parts of four individuals (A-D) for thermal verification: A – right arm, B – left arm, C – neck, and D – right leg. Specifically, the experiments for A, C and D are taken in an office room and the experiment for B is conducted in a sauna room. From the captured thermal images, thermal distributions including $T(\mathbf{x})$, $\tau(\mathbf{x})$ and $C(\mathbf{x})$ can be generated for all individuals (see the top row of Fig. 3 for an example). The thermal-comfort optimized casts are then computed by our approach. The results are compared with uniformly-sparse casts. To conduct a fair comparison, we produced uniformly-sparse casts that have the same area of air-exposure as the optimized casts. Here the uniformly-sparse casts are generated by using the traditional CVT algorithm (i.e., letting $\lambda = 0$ in Eq.(7)). The skin temperatures after wearing two casts are measured to make comparisons.

We fabricated an optimized cast as well as a uniformly-sparse cast for each participant and compared the thermal distribution on their body parts. The experiments were carried out after the participants entered the experimental rooms for 30 minutes. The uniformly-sparse cast was worn first, and then the optimized cast. During the experiments, participants sat still with only simple movements (e.g. reading and typing). The thermal images are taken after wearing the casts for 30 minutes. Note that more than an hour break was taken between two experiments to ensure the nude skin temperature drops to the same initial level (see the middle column of Fig. 11). Comparisons of skin-temperature distributions after wearing these casts are shown in Figs. 11, 12, 13 and 14 respectively. A lower temperature distribution due to ventilation given by optimized casts can be observed.
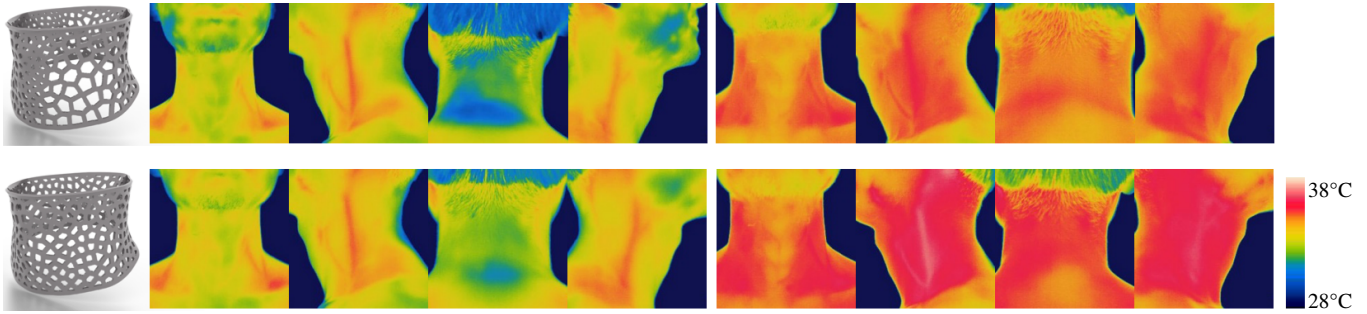
Figure 13. Comparison of temperature distribution after the participant C wearing an optimized cast (top row) vs. a uniformly-sparse cast (bottom) in an office room for 15 minutes – again, two casts have the same area of air-exposure.
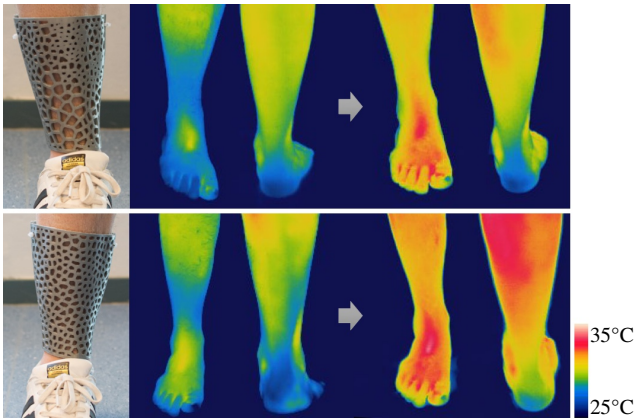

Figure 14. Comparison of temperature distribution after the participant D wearing an optimized cast (top) vs. a uniformly-sparse cast (bottom) in an office room for 30 minutes.

Figure 15. Thermal distribution of sample points on participant A, B, C and D after wearing the uniform and the optimized casts.

In order to quantitatively compare the temperature difference on the skin after wearing different casts (uniform vs. optimized), we sample the skins of participants into points in the thermal images and compare the histograms of temperature distribution (see Fig.15). When generating the histograms, 6,400 points (about 40% of the covered area) are sampled on the participant A's thermal images. Under the similar measurements, 4,000 samples, 4,500 samples and 7,200 samples are used for the case studies on the participants B, C and D respectively. Note that, the numbers of sample points used in each example are proportional to the areas of covered skins. All results can be found in Fig.15.

User Feedback We elicited feedback on the experience of the participants. All participants were asked to rate their experience on different aspects while wearing a fiberglass cast (fabricated by conventional production instead of 3D printing), a uniformly-sparse cast and an optimized cast – 3D printed. Responses are set on a 10-point scale regarding weight, appearance, thermal-comfort, tactility and facility. The questionnaire text was as follows:

Please rate from 1-10 (1 least agree, 10 most agree) what you think of the cast.
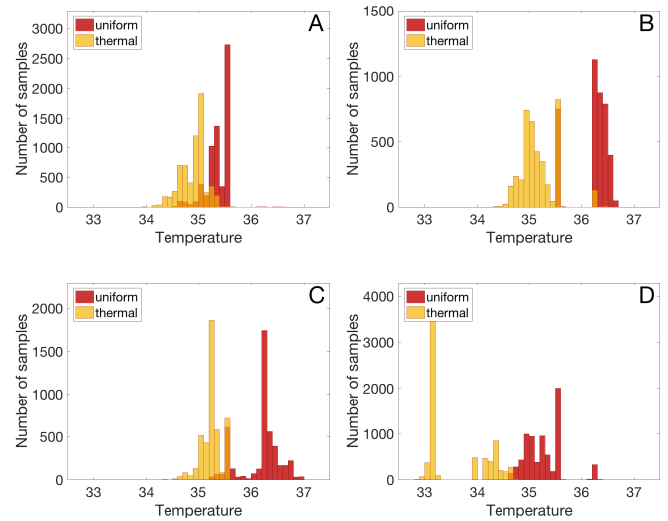
- *I think the cast is lightweight.*

- *I like the appearance of the cast.*

- *I feel thermally comfortable with the cast.*

- *I'm satisfied with the tactility of the cast.*

- *I'm satisfied with the facility of the cast. (Note, facility is an overall assessment of perception with the cast regarding regular activities, itchiness and its resistance to wear and tear)*

The feedback from four participants can be found in Fig. 16. Consistent with our main goal, all the optimized casts won the highest satisfactory score on thermal-comfort. On the other aspects, the weight discrepancy between 3D printed casts and fiberglass casts can be easily identified on large casts for the arms and legs. Facility scores showed that the optimized casts are eligible for daily usage. Comparing to fiberglass casts, 3D printed casts in general achieve lower scores on tactility and appearance. This can be boosted by adopting a more skin friendly material and choosing user preferred patterns.

In the experiments for the user study, all participants were excited by the appearance, functionality and easy prototyping of our optimized casts. At the same time, they all perceived and
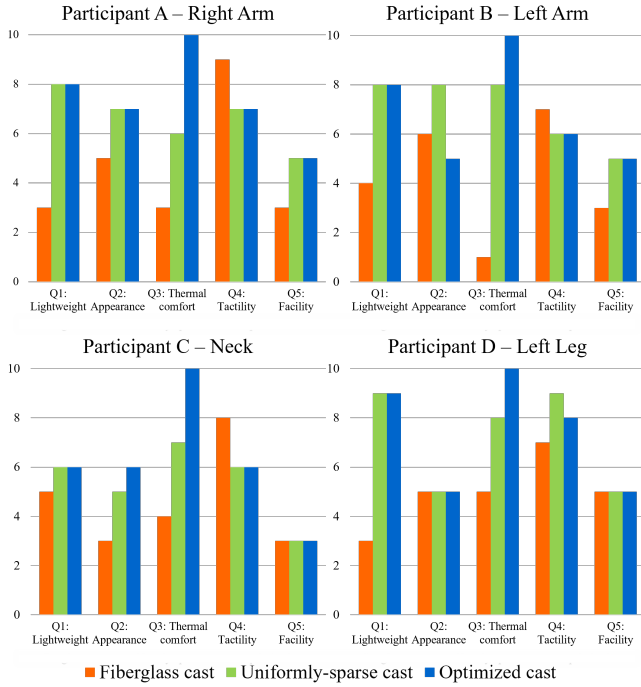
Figure 16. User feedback for all participants on weight, appearance, thermal-comfort, tactility and facility.
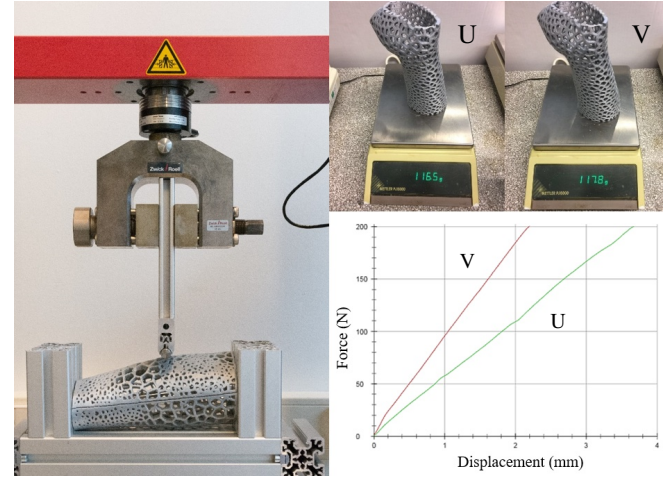

Figure 17. Mechanical validation on an optimized cast (V-curve in red color) with the same weight as a cast with uniform thickness (U-curve in green color) – the force-displacement curves show that the optimized cast has superior mechanical stiffness.

were displeased by the 'stuffy' and 'sweltering' experience with the conventional fiberglass casts. No similar complaints were made for either the uniformly-sparse casts or the optimized casts. In particular, participants A, B and D could also '*feel more ventilation*' with the optimized cast compared to the uniformly-sparse cast. All participants were surprised by the light weight of the 3D printed casts and in particular mentioned they were '*even lighter than my cell phone*'. On other aspects, they were all satisfied with the stiffness of the optimized casts – strong enough to support the human bodies. As criticism, participant C stated that the surface of a 3D printed cast is not smooth enough for delicate neck skin. He also suggested adding flared edges at the upper boundary of the cast to enlarge the supporting area for the head.

Heuristic Evaluation   We conducted a semi-structured interview with an orthopedic surgeon, in which both arm casts were presented and discussed. He agreed that thermal-comfort was a weakness with traditional casts and our samples clearly showed great promise together with making a custom-fit based on 3D scanning. The traditional approach of improving thermal-comfort is to make a one-sided cast and fix the arm with fabric, but this is only feasible in limited cases. Two challenges with our approach were foreseen by the expert: i) a patient cannot always attain a particular pose for 3D scanning (specifically concerning thumb injuries), which makes the scanning process difficult even when our handheld 3D scanner is used; ii) the current printing material and method results in unsatisfactory tactile-comfort, which could be improved by using softer material and a 3D printer with higher resolution (also discussed in future work). Furthermore, the expert indicated that some finishing would be required. Specifically,

at the bottom of the printed models, the sharp ridges could protrude in the arm (also discussed in user tests).

Mechanical Verification   Mechanical tests are conducted to validate our approach in enhancing mechanical stiffness by non-uniform thickening. As shown in Fig. 17, the tests are given on two models V and U, where the model V is a cast with non-uniform thickness (between 4 and 6mm) optimized by our method and the model U is a cast generated by using uniform thickness (4.4mm). Both having nearly the same weight ($W_V = 117.8$g, $W_U = 116.5$g). The mechanical stiffness tests are taken on a Zwick Roell static testing machine by applying forces up to 200N. The measured force-displacement curves are shown in Fig. 17. The optimized cast has a much steeper curve, meaning that it has superior mechanical stiffness.

Computational Performance   Our computation consists of three steps: 1) pattern optimization, 2) HVT-based mesh generation, and 3) structural enhancement by non-uniform thickening. In all our experiments, mesh surfaces with approximately 120k triangles are used. The total time of computation ranges from 40 to 150 minutes (with $n = 1,000$ and $r = 1.5$mm). The performance bottleneck is pattern optimization, approximately 95% of computation time is spent on this step, which also depends on the value of the contrast coefficient λ. When a larger λ is used, our approach will result in a HVT with more significant size variation between regions, leading to more iterations. For example, when increasing the value of λ from 15 to 135 on the forearm cast, the computation time increases nearly 4 times. Moreover, computing time is also affected by the distribution of thermal-comfort sensitivity. Computation on uniform distributions converges faster. The top row of Fig. 18 shows the temperature distributions $T(\mathbf{x})$ and $\tau(\mathbf{x})$ obtained from Fig. 9 and the corresponding thermal-comfort sensitivity $C(\mathbf{x})$. The results of web-like casts using different contrast coefficients are given at the bottom row of Fig. 18.
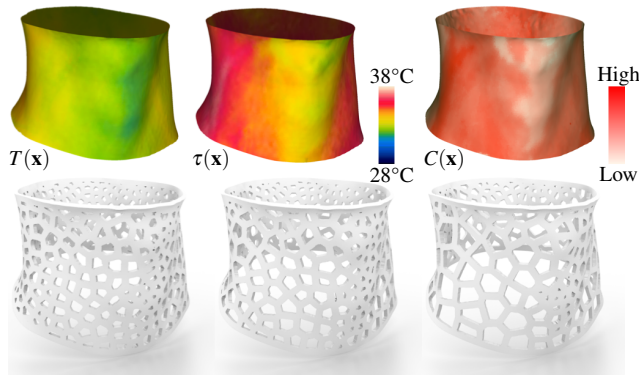
Figure 18. Results of a thermal-comfort aware cast for the neck. (Top row) thermal distributions generated on the neck surface. (Bottom row) web-like casts resulting from different contrast coefficients (left to right: $\lambda = \{50, 75, 125\}$).

CONCLUSION

We have presented a novel computational paradigm for addressing the thermal-comfort design problem on personalized casts. Specifically, a pattern of HVT has been employed for designing the web-like casts. A discrete optimization method is developed to generate patterns for web-like casts maximizing the thermal-comfort of users. To simultaneously satisfy the requirement on mechanical stiffness, a structural optimization method is introduced by varying the thickness of shell at high stress regions according to the simulation results of FEA. Our approach has been implemented and verified on a few personalized casts for different individuals. Experimental results are very encouraging – in addition to positive user feedback, both the thermal-comfort (shown in temperature variation) and the mechanical stiffness (shown in stress-strain curve) have been clearly enhanced on the optimized casts generated by our approach.

Limitations and Future Work Although the thermal-comfort of wearable devices can be influenced by multiple factors (such as materials, interface, etc.), we focus on enhancing the exposure of skin to air in the regions with high thermal sensitivity – i.e., a geometric solution. This solution can be combined with material or mechatronics solutions to further improve the performance of ventilation to covered skins. A desktop 3D printer with PLA material is used to fabricate the casts, which could be abrasive if worn for long periods. This situation would be improved by using polypropylene material as suggested in [27] where no extra padding is needed. Studies have shown that polypropylene exhibits no adverse effects and is biocompatible [39]. Moreover, polypropylene is even lighter (946 kg/m^3) compared to PLA (1250 kg/m^3).

In our current implementation, thermal images are taken from four orthogonal directions covering the whole fractured body. The images are converted into 2D temperature distributions and then mapped onto the 3D shape obtained from a 3D scanner. The mapping process involves tedious manual operations. We planned to develop a new scanning device that can capture the 3D geometry and the temperature distribution in the same shot. Another interesting research in the future is to take

the clinic study about whether there is significant difference between thermal images of a healthy person and a body with bone-fracture. Thermal images might show abnormalities due to different blood flow on an injured body.

Although 3D printed casts are used as a main application in this paper, our method has a great potential to be further extended in other applications. Many wearable products could be facilitated by considering customized thermal-comfort – e.g., interactively designed dresses [49], wearable haptic systems [8] or car seats [26]. From the technical aspect, our pattern optimization algorithm can be modified according to different objectives in other interactive design tools such as styled pattern design [10] and multi-material design for soft robotics [44].

REFERENCES
1. E. Arens and H. Zhang. 2006. The skin's role in human thermoregulation and comfort. *Center for the Built Environment* (2006).

2. E. Arens, H. Zhang, and C. Huizenga. 2006. Partial-and whole-body thermal sensation and comfort – Part I: Uniform environmental conditions. *Journal of thermal Biology* 31, 1 (2006), 53–59.

3. ASHRAE. 2001. Fundamentals. *American Society of Heating, Refrigerating and Air Conditioning Engineers, Atlanta* 111 (2001).

4. M. Attia and P. Engel. 1981. Thermal alliesthesial response in man is independent of skin location stimulated. *Physiology & behavior* 27, 3 (1981), 439–444.

5. S. Axler, P. Bourdon, and R. Wade. 2013. *Harmonic function theory*. Vol. 137. Springer Science & Business Media.

6. P. Baudisch and S. Mueller. 2016. Personal Fabrication: State of the Art and Future Research. In *Proceedings of the 2016 CHI Conference Extended Abstracts on Human Factors in Computing Systems*. ACM, 936–939.

7. T.N. Bitzer. 2012. *Honeycomb technology: materials, design, manufacturing, applications and testing*. Springer Science & Business Media.

8. L. Bonanni, C. Vaucelle, J. Lieberman, and O. Zuckerman. 2006. TapTap: a haptic wearable for asynchronous distributed touch therapy. In *CHI'06 extended abstracts on Human factors in computing systems*. ACM, 580–585.

9. Desai Chen, David IW Levin, Shinjiro Sueda, and Wojciech Matusik. 2015. Data-driven finite elements for

geometry and material design. *ACM Transactions on Graphics (TOG)* 34, 4 (2015), 74.

10. W. Chen, X. Zhang, S. Xin, Y. Xia, S. Lefebvre, and W. Wang. 2016. Synthesis of filigrees for digital fabrication. *ACM Transactions on Graphics (TOG)* 35, 4 (2016), 98.

11. K. Dai, M. Yan, Z. Zhu, and Y. Sun. 2007. Computer-aided custom-made hemipelvic prosthesis used in extensive pelvic lesions. *The Journal of arthroplasty* 22, 7 (2007), 981–986.

12. Q. Du, V. Faber, and M. Gunzburger. 1999. Centroidal Voronoi tessellations: applications and algorithms. *SIAM review* 41, 4 (1999), 637–676.

13. J. Dumas, A. Lu, S. Lefebvre, J. Wu, and C. Dick. 2015. By-example synthesis of structurally sound patterns. *ACM Transactions on Graphics (TOG)* 34, 4 (2015), 137.

14. J. Evill. 2016. Cortex: Exoskeletal Cast. `http://www.evilldesign.com/cortex`. (2016).

15. A.P. Gagge, J.A.J. Stolwijk, and J.D. Hardy. 1967. Comfort and thermal sensations and associated physiological responses at various ambient temperatures. *Environmental research* 1, 1 (1967), 1–20.

16. M. Gannon, T. Grossman, and G. Fitzmaurice. 2015. Tactum: a skin-centric approach to digital design and fabrication. In *Proceedings of the 33rd Annual ACM Conference on Human Factors in Computing Systems*. ACM, 1779–1788.

17. M. Gannon, T. Grossman, and G. Fitzmaurice. 2016. ExoSkin: On-body fabrication. In *Proceedings of the 2016 CHI Conference on Human Factors in Computing Systems*. ACM, 5996–6007.

18. C. Hurson, A. Tansey, B. O'donnchadha, P. Nicholson, J. Rice, and J. McElwain. 2007. Rapid prototyping in the assessment, classification and preoperative planning of acetabular fractures. *Injury* 38, 10 (2007), 1158–1162.

19. T. Ju, F. Losasso, S. Schaefer, and J. Warren. 2002. Dual Contouring of Hermite Data. *ACM Trans. Graph.* 21, 3 (July 2002), 339–346. DOI: `http://dx.doi.org/10.1145/566654.566586`

20. D. Karasahin. 2014. Osteoid Medical cast. `https://competition.adesignaward.com/design.php?ID=34151`. (2014).

21. H. Kim and S. Jeong. 2015. Case study: Hybrid model for the customized wrist orthosis using 3D printing. *Journal of Mechanical Science and Technology* 29, 12 (2015), 5151–5156.

22. T. Langlois, A. Shamir, D. Dror, W. Matusik, and D. I. W. Levin. 2016. Stochastic Structural Analysis for Context-aware Design and Fabrication. *ACM Trans. Graph.* 35, 6, Article 226 (Nov. 2016), 13 pages. DOI: `http://dx.doi.org/10.1145/2980179.2982436`

23. G. Laput, X. Chen, and C. Harrison. 2015. 3D printed hair: Fused deposition modeling of soft strands, fibers, and bristles. In *Proceedings of the 28th Annual ACM Symposium on User Interface Software & Technology*. ACM, 593–597.

24. S. Lautenbacher and F. Strian. 1991. Sex differences in pain and thermal sensitivity: the role of body size. *Attention, Perception, & Psychophysics* 50, 2 (1991), 179–183.

25. B. Lévy and Y. Liu. 2010. Lp Centroidal Voronoi Tessellation and Its Applications. *ACM Trans. Graph.* 29, 4, Article 119 (July 2010), 11 pages. DOI: `http://dx.doi.org/10.1145/1778765.1778856`

26. Lexus. 2016. Lexus Kinetic Seat Concept World Premiere at the 2016 Paris Motor Show. `http://pressroom.lexus.com/releases/lexus-kinetic-seat-concept-premiere-2016-paris-motor-show.htm`. (2016).

27. H. Lin, L. Shi, and D. Wang. 2016. A rapid and intelligent designing technique for patient-specific and 3D-printed orthopedic cast. *3D Printing in Medicine* 2, 1 (2016), 4.

28. S. Lloyd. 1982. Least squares quantization in PCM. *IEEE transactions on information theory* 28, 2 (1982), 129–137.

29. W.E. Lorensen and H.E. Cline. 1987. Marching Cubes: A High Resolution 3D Surface Construction Algorithm. In *Proceedings of SIGGRAPH '87*. 7. DOI: `http://dx.doi.org/10.1145/37401.37422`

30. L. Lu, A. Sharf, H. Zhao, Y. Wei, Q. Fan, X. Chen, Y. Savoye, C. Tu, D. Cohen-Or, and B. Chen. 2014. Build-to-last: strength to weight 3D printed objects. *ACM Transactions on Graphics (TOG)* 33, 4 (2014), 97.

31. J. Martínez, J. Dumas, and S. Lefebvre. 2016. Procedural Voronoi Foams for Additive Manufacturing. *ACM Trans. Graph.* 35, 4, Article 44 (July 2016), 12 pages. DOI: `http://dx.doi.org/10.1145/2897824.2925922`

32. J. Martínez, J. Dumas, S. Lefebvre, and L. Wei. 2015. Structure and appearance optimization for controllable shape design. *ACM Transactions on Graphics (TOG)* 34, 6 (2015), 229.

33. C. Mavroidis, R.G. Ranky, M.L. Sivak, B.L. Patritti, J. DiPisa, A. Caddle, K. Gilhooly, L. Govoni, S. Sivak, M. Lancia, and others. 2011. Patient specific ankle-foot orthoses using rapid prototyping. *Journal of neuroengineering and rehabilitation* 8, 1 (2011), 1.

34. G.D. Mower. 1976. Perceived intensity of peripheral thermal stimuli is independent of internal body temperature. *Journal of comparative and physiological psychology* 90, 12 (1976), 1152.

35. S. Mueller, S. Im, S. Gurevich, A. Teibrich, L. Pfisterer, F. Guimbretière, and P. Baudisch. 2014a. WirePrint: Fast 3D printed previews. *Proc. UIST'14* (2014), 273–280.

36. S. Mueller, T. Mohr, K. Guenther, J. Frohnhofen, and P. Baudisch. 2014b. faBrickation: fast 3D printing of functional objects by integrating construction kit building blocks. In *Proceedings of the 32nd annual ACM conference on Human factors in computing systems*. ACM, 3827–3834.

37. P. Musialski, C. Hafner, F. Rist, M. Birsak, M. Wimmer, and L. Kobbelt. 2016. Non-linear Shape Optimization Using Local Subspace Projections. *ACM Trans. Graph.* 35, 4, Article 87 (July 2016), 13 pages. DOI: `http://dx.doi.org/10.1145/2897824.2925886`

38. J. Panetta, Q. Zhou, L. Malomo, N. Pietroni, P. Cignoni, and D. Zorin. 2015. Elastic textures for additive fabrication. *ACM Transactions on Graphics (TOG)* 34, 4 (2015), 135.

39. V. Sastri. 2013. *Plastics in medical devices: properties, requirements, and applications*. William Andrew.

40. V. Savage, S. Follmer, J. Li, and B. Hartmann. 2015. Makers' Marks: Physical markup for designing and fabricating functional objects. In *Proceedings of the 28th Annual ACM Symposium on User Interface Software & Technology*. ACM, 103–108.

41. C. Schumacher, B. Bickel, J. Rys, S. Marschner, C. Daraio, and M. Gross. 2015. Microstructures to control elasticity in 3D printing. *ACM Transactions on Graphics (TOG)* 34, 4 (2015), 136.

42. C. Schumacher, B. Thomaszewski, and M. Gross. 2016. Stenciling: Designing Structurally-Sound Surfaces with Decorative Patterns. *Computer Graphics Forum* 35, 5 (2016), 101–110.

43. J. Schuren. 1994. *Working with soft cast: a manual on semi-rigid immobilisation*. Minnesota Mining & Manufacturing.

44. M. Skouras, B. Thomaszewski, S. Coros, B. Bickel, and M. Gross. 2013. Computational design of actuated deformable characters. *ACM Transactions on Graphics (TOG)* 32, 4 (2013), 82.

45. A. Teibrich, S. Mueller, F. Guimbretière, R. Kovacs, S. Neubert, and P. Baudisch. 2015. Patching physical objects. In *Proceedings of the 28th Annual ACM Symposium on User Interface Software & Technology*. ACM, 83–91.

46. C. Torres, T. Campbell, N. Kumar, and E. Paulos. 2015. HapticPrint: Designing feel aesthetics for digital fabrication. In *Proceedings of the 28th Annual ACM Symposium on User Interface Software & Technology*. ACM, 583–591.

47. C.C.L. Wang and Y. Chen. 2013. Thickening freeform surfaces for solid fabrication. *Rapid Prototyping Journal* 19, 6 (2013), 395–406.

48. W. Wang, T.Y. Wang, Z. Yang, L. Liu, X. Tong, W. Tong, J. Deng, F. Chen, and X. Liu. 2013. Cost-effective printing of 3D objects with skin-frame structures. *ACM Transactions on Graphics (TOG)* 32, 6 (2013), 177.

49. A. Wibowo, D. Sakamoto, J. Mitani, and T. Igarashi. 2012. DressUp: a 3D interface for clothing design with a physical mannequin. In *Proceedings of the Sixth International Conference on Tangible, Embedded and Embodied Interaction*. ACM, 99–102.

50. K. Wong, S. Kumta, K. Sze, and C. Wong. 2012. Use of a patient-specific CAD/CAM surgical jig in extremity bone tumor resection and custom prosthetic reconstruction. *Computer Aided Surgery* 17, 6 (2012), 284–293.

51. J. Wu, C. Dick, and R. Westermann. 2016a. A System for High-Resolution Topology Optimization. *IEEE Transactions on Visualization and Computer Graphics* 22, 3 (2016), 1195–1208. DOI: `http://dx.doi.org/10.1109/TVCG.2015.2502588`

52. J. Wu, C.C.L. Wang, X. Zhang, and R. Westermann. 2016b. Self-supporting rhombic infill structures for additive manufacturing. *Computer-Aided Design* 80 (2016), 32 – 42. DOI: `http://dx.doi.org/10.1016/j.cad.2016.07.006`

53. J. Zehnder, S. Coros, and B. Thomaszewski. 2016. Designing structurally-sound ornamental curve networks. *ACM Transactions on Graphics (TOG)* 35, 4 (2016), 99.

54. H. Zhang, E. Arens, C. Huizenga, and T. Han. 2010a. Thermal sensation and comfort models for non-uniform and transient environments: Part I: Local sensation of individual body parts. *Building and Environment* 45, 2 (2010), 380–388.

55. H. Zhang, E. Arens, C. Huizenga, and T. Han. 2010b. Thermal sensation and comfort models for non-uniform and transient environments, part II: Local comfort of individual body parts. *Building and Environment* 45, 2 (2010), 389–398.

56. Q. Zhou, J. Panetta, and D. Zorin. 2013. Worst-case Structural Analysis. *ACM Trans. Graph.* 32, 4, Article 137 (July 2013), 12 pages. DOI: `http://dx.doi.org/10.1145/2461912.2461967`